Development of a Second Order Dynamic Stall Model

Niels Adema[1], Menno Kloosterman[2], Gerard Schepers[1]

[1]EUREC European Master in Renewable Energy, Hanze University of Applied Sciences, Groningen, 9747 AS, The Netherlands

5 [2]DNV GL, Groningen, 9743 AN, The Netherlands

Correspondence to: Adema N.C. Niels (nielsadema1994@gmail.com)

Abstract. Dynamic stall phenomena bring risk for negative damping and instability in wind turbine blades. It is crucial to model these phenomena accurately to reduce inaccuracies in predicting design driving (fatigue) loads. Inaccuracies in current dynamic stall models may be due to the facts that they are not properly designed for high angles of attack, and that they do not

10 specifically describe vortex shedding behaviour. The Snel second order dynamic stall model attempts to explicitly model unsteady vortex shedding. This model could therefore be a valuable addition to DNV GL's turbine design software Bladed. In this thesis the model has been validated with oscillating airfoil experiments and improvements have been proposed for reducing inaccuracies. The proposed changes led to an overall reduction in error between the model and experimental data. Furthermore the vibration frequency prediction improved significantly. The improved model has been implemented in Bladed and tested

15 against small scale turbine experiments at parked conditions. At high angles of attack the model looks promising for reducing mismatches between predicated and measured (fatigue) loading. Leading to possible lower safety factors for design and more cost efficient designs for future wind turbines.

1 Introduction

Wind turbines operate in highly unsteady aerodynamic environments (Leishman, 2002). For design and certification design

20 load cases (DLC's) have been set which describe the conditions which turbine design have to withstand (DNV GL, 2016). The design driving DLC's are those for parked and idling conditions where wind turbine blades will experience high angles of attack (AoA), leading to (dynamic) stall behaviour (Schreck et al., 2000). The wind turbine yaw angle is defined as the angle in the horizontal plane between the free stream wind direction and the wind turbine rotor shaft. It can be noted that when the turbine is parked, and the blades pitched to 90°, the yaw angle effectively becomes the inflow angle. When the yaw system is

25 not operating during parked conditions due to a failure, the blades will experience flow from all direction. For particular wind directions the flow on the blades is separated leading to dynamic stall effects. Accurate modelling of dynamic stall is therefore crucial in wind turbine design (Choudry et al., 2014).

Dynamic stall is a phenomenon leading to larger variations in lift, drag and pitching moments on the airfoil than would be observed during steady operation (Choudry et al., 2014). This, in case, creates larger aerodynamic forces on the blades than

30 expected during steady condition (Leishman, 2002). Dynamic stall can be viewed as a delay in the onset of stall. Recirculation

of flow after the static stall angle starts near the trailing edge and rapidly moves towards the leading edge. Leading to the formation of a large dynamic stall clockwise vortex at the leading edge at increasing angles of attack. The dynamic stall vortex will travel along the suction side from the leading towards the trailing edge before detaching completely. Full separation will occur when the dynamic stall vortex is completely detached. This moment is called the 'break' or 'dynamic stall onset'. After

35   that sudden drop in lift the airfoil will return to low angles of attack due to the loss of lift and pitching down motion. However, a time delay for reattachment of the flow is present as well. After reattachment the process repeats creating a hysteresis loop. Dynamic stall phenomena bring risk for negative damping and instability. Especially if the airfoil is oscillating in and out of stall (McCroskey, 1981). A visual description for dynamic stall is presented in figure (1).
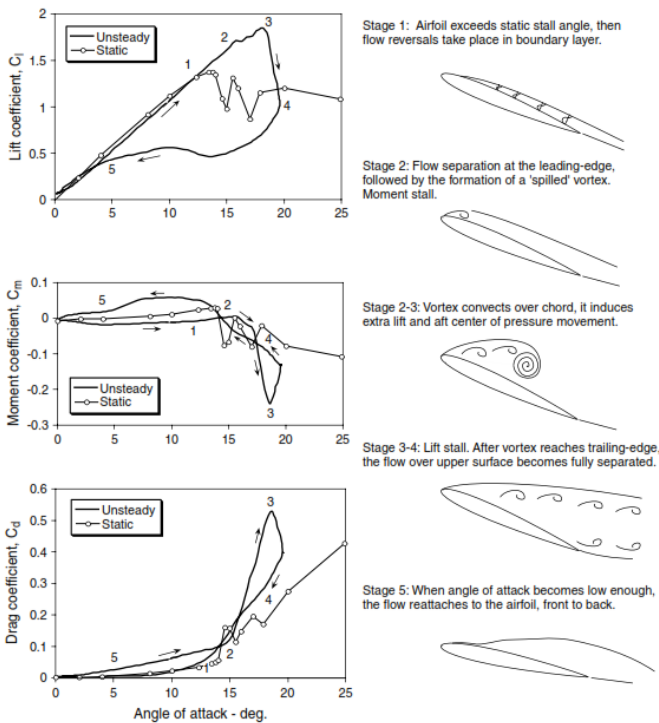
40   **Figure 1: Classical Visual Representation of Dynamic Stall (Leishman, 2002)**

When keeping the airfoil pitched in (deep) stall for longer periods of time, periodic vortex shedding will occur. No longer a single large dynamic stall vortex will be shed but multiple periodic vortices from both the leading and trailing edge. This will induce time varying loads on the blades (Riziotis et al., 2010). The periodic vortex shedding is characterised by the Strouhal number representing the dimensionless frequency of shedding (Pellegrino and Meskell, 2013). The Strouhal number is defined

45   following Eq. (1):

$$St = \frac{f*c}{U}, \tag{1}$$

In which f notes the characteristic vortex shedding frequency, c the airfoil chord (sometimes the projected chord length perpendicular to the incoming flow), and U the wind velocity at the wind turbine blade section. Synchronization of the natural

and Strouhal frequencies (a "lock-in") will lead to resonance (Pellegrino and Meskell, 2013). Locked-in vortex induced vibrations are a potential threat in standstill conditions as the turbine size is increasing. Modern aeroelastic tools with dynamic stall models are only able to provide accurate deep stall loads at conditions close to maximal lift, so relative small angles of attack (Riziotis et al., 2010). The same study noted that today's aeroelastic tools are not properly tuned for high angles of attack. Mismatches between load predictions between measurements and engineering tools have found to be as high as 20% for high wind speed dynamic stall conditions (Schreck, 2002). State of the art aerodynamic models overestimate fatigue loading with 15% (Schepers and Snel, 2007). Modern day computational fluid dynamics (CFD) are becoming more able to accurately predict dynamic stall behaviour but require large computational power, therefore they are not fit for practical design calculations. In the industry there is a need for relatively fast and accurate engineering models predicting key loading. The inaccuracies in dynamic stall models may be due to the above described facts that they are not properly designed for high angles of attack, and that they do not specifically describe vortex shedding behaviour.

The Snel second order dynamic stall model attempts to explicitly model unsteady vortex shedding. This model is currently not applied in DNV GL's turbine design tool Bladed and could be a valuable addition to the dynamic stall module of Bladed. However, a need for further tuning and validation of the model is still required (Snel 1997). This thesis will provide a detailed analysis into the Snel second order model and will try to answer the following main research question:

What are possible ways to improve predictions of blade vibrations during dynamic stall in parked conditions using the Snel second order model?

2. Methodology

This paper will have the following methodology:

- The Snel model is validated with experimental data.
- Proposed changes are presented based on the validation results to improve the model predictions.
- Attention will be paid to vibration prediction as this influences turbine fatigue loading which has a large impact on the design of the wind turbine.
- An absolute error analysis is carried out before and after the improvements to quantify the increase in performance.
- The improved model will be tested with actual small scale turbine experimental data to assess performance in combination with Bladed.

3. Detailed Analysis of the Snel Second Order Model

This chapter will validate the Snel model and propose adaptations to the model to improve the performance. (Snel, 1993) derived a dynamic stall model based on the work of (Truong, 1993) who proposed that the dynamic lift coefficient can be distinguished in two parts. The first describes the forcing frequency response and the second term the self-exited higher

frequency dynamics. Snel follows this approach but also expresses the first part as the difference from the steady state (time

80 averaged) lift coefficient (Montgomerie, 1996). The dynamic lift of the Snel model will be as in Eq. (2). The first part, Δc_{l1},

must decay to zero when no excitation is present while the second part will decay to zero for small angles of attack, but nearing

stall the second part will show periodic oscillations related to vortex shedding.

$$c_{l,dyn} = c_{l,steady} + \Delta c_{l1} + \Delta c_{l2} \,, \tag{2}$$

In the original model of Truong the first part is based on the Beddoes-Leishman dynamic stall model. The Snel model uses the

85 SIMPLE (Montgomerie, 1996) as a departure point for the first order correction while (Truong, 1993) uses the B-L model to

calculate Δc_{l1}. The modelling of the first part will therefore follow:

$$\tau \Delta \mathrm{c}_{l1} + cf_{10} \Delta c_{l1} = ft_1 \,, \tag{3}$$

The forcing term ft_1 will be based on the time derivative of the difference between the steady and potential lift coefficient.

This is shown in Eq. (4) and (5). The function is made non-dimensional by taking the coefficient of the derivative term as the

90 time constant usually used in dynamic stall. This constant is described in Eq. (11).

$$ft_1 = \tau \Delta \dot{c}_{l,pot} \,, \tag{4}$$

$$\Delta c_{l,pot} = c_{l,pot} - c_{l,steady} = 2\pi \sin(\alpha - \alpha_0) - c_{l,steady} \,, \tag{5}$$

The coefficient of Δc_{l1} can be seen as a spring trying to pull the term back to the steady state of zero. The stiffness of the spring

of this equation is given by Eq. (6). In downwards pitching motion the stiffness is higher than in upwards pitching motion.

95 $$cf_{10} = \begin{cases} \dfrac{1+0.5\Delta c_{l,pot}}{8(1+60\tau\dot{\alpha})} & if\ \dot{\alpha}c_{l,pot} \le 0 \\ \dfrac{1+0.5\Delta c_{l,pot}}{8(1+80\tau\dot{\alpha})} & if\ \dot{\alpha}c_{l,pot} > 0 \end{cases}, \tag{6}$$

The second part of the dynamic lift coefficient is of second order to create the higher frequency dynamics. This will be a non-

linear mass-damper-spring system following:

$$\tau^2 \Delta \ddot{c}_{l2} + cf_{21} \Delta \dot{c}_{l2} + cf_{20} \Delta c_{l2} = ft_2 \,, \tag{7}$$

The spring and damping coefficients are taken from (Snel, 1997) and are defined as in Eq. (8) and (9) respectively.

100 $$cf_{20} = k_s^2 [1 + 3(\Delta c_{l2})^2][1 + 3\dot{\alpha}^2] \,, \tag{8}$$

$$cf_{21} = \begin{cases} 60\tau k_s [-0.01(\Delta c_{l,pot} - 0.5) + 2(\Delta c_{l2})^2] & if\ \dot{\alpha} > 0 \\ 2\tau k_s & if\ \dot{\alpha} \le 0 \end{cases}, \tag{9}$$

Also here it can be noted that the response will be different for pitching upwards or downwards. The forcing term is defined

as:

$$ft_2 = 0.1k_s(-0.15\Delta c_{l,pot} + 0.05\Delta \dot{c}_{l,pot}), \tag{10}$$

105 In the second order part of the model k_s is taken as the reduced vortex shedding frequency or Strouhal number. This is given

a value of 0.2 as in the original model (Snel, 1997) In the above equations the time constant is given as Eq. (11) and can be

seen as the time it takes for the wind to travel half a chord distance:

$$\tau = c/2U, \qquad\qquad (11)$$

The Ohio State University (OSU) experiments (Hoffmann et al., 1996) will be used for validation of the initial implementation

110 of the Snel model. In the OSU experiments an extensive set of airfoils have been tested for both unsteady and steady data. The measurements recorded responses to forced sinusoidal pitching oscillations. Different amplitudes, mean angles of attack, oscillation frequencies and Reynolds numbers were tested. The focus in this thesis will be on the NACA4415 and S809 Airfoils. The model parameters obtained from the OSU database, as displayed in table (1), will be analyzed.

Airfoil	# Test Case	Mean wind Speed [m/s]	Average Angle of Attack [deg]	Amplitude [deg]	Oscillation Frequency [Hz]
S809	1	42.8	8.1	10.2	0.60
	2	43.0	8.2	10.1	1.20
	3	42.7	8.3	10.2	1.89
	4	42.8	13.2	10.4	0.60
	5	41.7	12.9	10.1	1.22
	6	42.0	12.9	10.1	1.81
	7	42.3	18.8	10.2	0.61
	8	42.1	18.8	10.1	1.18
	9	42.6	18.7	10.0	1.84
NACA 4415	11	37.9	7.0	11.2	0.61
	12	37.9	7.5	10.8	1.20
	13	37.8	7.3	10.7	1.85
	14	37.8	14.0	10.5	0.60
	15	37.7	14.1	10.6	1.22
	16	37.3	14.1	10.6	1.81
	17	37.2	18.6	10.5	0.61
	18	37.1	18.3	10.8	1.24
	19	37.2	18.4	10.7	1.84

115 **Table 1: Selected cases from the OSU Experiments**

3.1 Initial Model Implementation and Validation

The Snel model as in described in chapter 3 is implemented in a MATLAB environment. The numerical implementation follows the steps described in (de Vaal, 2009). The selected timestep is 0.001 seconds. The oscillation frequencies of the cases are set such that the forcing angle of attack matches the OSU data as good as possible. Figures (2) and (3) show the time series

120 of the lift coefficient for cases with both low and high reduced frequencies, low and high mean angles of attack. The followng observations can been made for the current model:

- - The current model under predicts the downstroke.
- - The predicted vortex shedding does not always happen at the correct time.
- - There is currently no unsteady vortex shedding at higher angles of attack as the model uses steady lift data only,
125   which tends to zero at 90° angle of attack.
- - The shedding frequency is not dependent on the reduced frequency while the experiments do show a dependency.

These points will be analysed as part of the possible improvements described in chapters 3.3 up to 3.9.
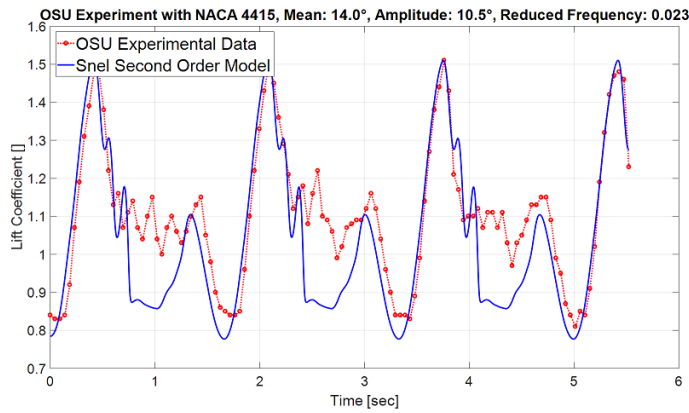
Figure 2: Lift coefficient time of the initial Snel model (NACA 4415 Airfoil at low reduced frequency)
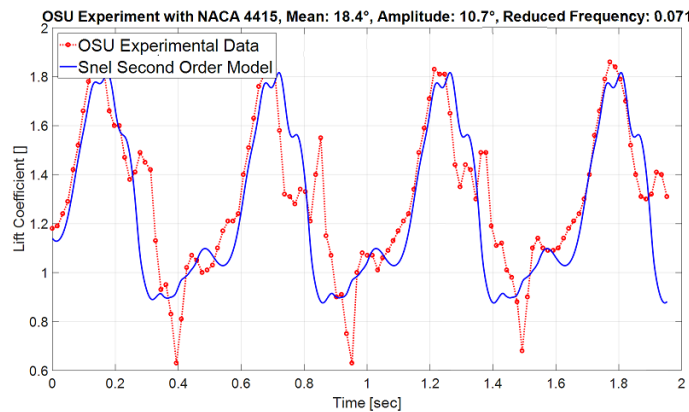
130

Figure 3: Lift coefficient time of the initial Snel model (NACA 4415 Airfoil at high reduced frequency)

3.2 Error Analysis

To quantify the accuracy of the Snel model, the total absolute error between model and experiments is calculated. This will give an objective measure to estimate proposed improvements. The Snel model is interpolated along the Angle of Attack to
135   obtain the dynamic lift coefficient output at the precise angles of attack of the OSU Experiment. The errors are then evaluated

according to Eq. (12). And the total absolute error of all datapoints is calculated using Eq. (13) in which n denotes the number of datapoint of the OSU experiment.

$$E_i = c_{l,model}(\alpha_i) - c_{l,OSU}(\alpha_i), \tag{12}$$

$$Absolute\ Error = \sqrt{\frac{1}{n} \sum_{i=1}^{n} E_i^2}, \tag{13}$$

3.3 Dimensional Analysis

It can be seen in the formulation of the model that Eq. (8) and (10) are cast in a dimensional form. For different values for chords, wind speed and pitching frequency the current model will not produce identical results. In order to make them dimensionless, the time constant used in dynamic stall (Eq. (11)) will be added. The new constants will be such that the initial value of the constant is kept. The equations will now be as Eq. (14) and (15).

$$cf_{20} = k_s^2[1 + 3(\Delta c_{l2})^2][1 + 280^2\tau^2\dot{\alpha}^2], \tag{14}$$

$$ft_2 = 0.1k_s(-0.15\Delta c_{l,pot} + 8\tau\Delta\dot{c}_{l,pot}), \tag{15}$$

3.4 Correct Slope for Cl potential

The Snel model uses 2π as theoretical slope for lift coefficient at low angles of attack. This theoretical value might not be applicable to real airfoils. Calculating the precise slope may improve the accuracy of the model. Therefore the slope calculated from the airfoil polar is used in the model. The slope will be calculated between the intercept at angle of attack = 0 and the intercept at lift coefficient = 0.

3.5 Application of the Normal Force Coefficient

The Snel model uses of the steady airfoil data. The lift coefficient tends to zero when angles of attack reach 90°. At 90° angle of attack however, there is still unsteady vortex shedding. Therefore, it would make sense to model vortex shedding to the normal force on the airfoil. The normal force coefficient together with the lift coefficient is presented in figure 4. First the normal force will follow the lift force up to stall. When the angle of attack increases the normal force coefficient gets composed of both the lift and drag and at 90° the normal force coefficient will be predominantly driven by the drag force as the lift is almost zero. The implementation of the normal force coefficient can be seen in chapter 3.10.
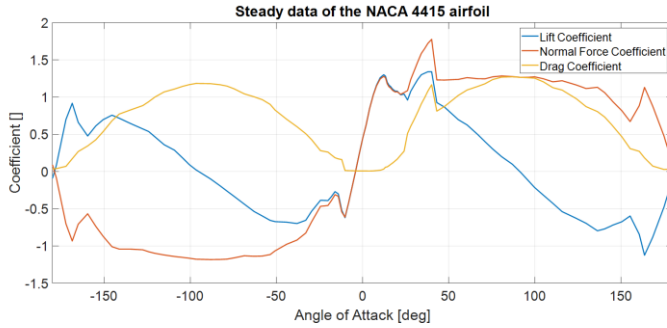
160   **Figure 4: Steady Polars of the NACA 4415 Airfoil**

3.6 Downstroke of the Model

The consistent differences between the implementation of the Snel second order model and earlier implementations are lower values in the downstroke. Figure (5) shows the first and second order part of the model as function of time. The second order part (Δc_{l2}) contributes highly to the lower values at the start of the downstroke which causes a large part of the observed error.

165   Eq. (10) uses $-0.15\Delta c_{l,pot}$. Together with a negative $\Delta \dot{c}_{l,pot}$ in the downstroke, ft_2 will be very negative in the downstroke. To improve this behaviour the forcing term is set to zero for the downstroke. Besides, figures (2) and (3) show that the predicted shedding in the upstroke is larger than in the measurments. Thereto the forcing term is lowered and will change to Eq. (16).

$$ft_2 = 0.1 k_s\left(-0.08\Delta c_{l,pot} + 1.5\tau\Delta\dot{c}_{l,pot}\right),\tag{16}$$

From figures (1) and (2) it is visible that there are vibrations in the downstroke. This is not modelled as cf_{21} is a constant value
170   in the downstroke, see Eq. (9). To allow shedding the coeffcient will be changed to Eq. (17). The damping in the downstroke is set higher than in the upstroke.

$$cf_{21} = \begin{cases} 60\tau k_s\left[-0.01\left(\Delta c_{n,pot} - 0.5\right) + 2\left(\Delta c_{n2}\right)^2\right] & if\ \dot{\alpha} > 0 \\ 60\tau k_s\left[-0.01\left(\Delta c_{n,pot} - 0.5\right) + 12\left(\Delta c_{n2}\right)^2\right] & if\ \dot{\alpha} \le 0 \end{cases},\tag{17}$$
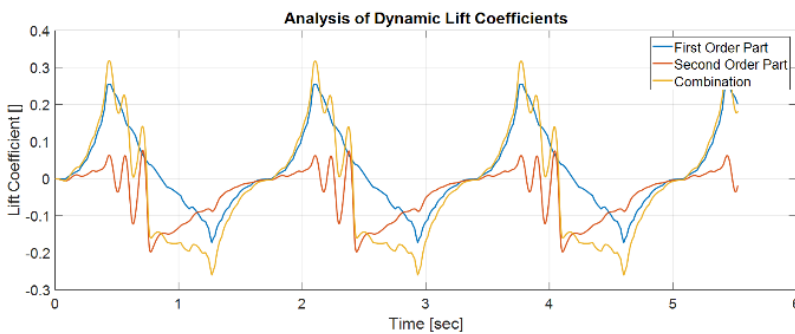
175   **Figure 5: Analysis of the dynamic lift coefficient**

3.7 Prediction of Vortex Shedding

The shedding frequency will depend on the angle of attack. The current model does not predict a dependency and so it has to be improved in this aspect. The Strouhal number uses the chord or the projected chord perpendicular to the incoming flow. Because the projected chord length is driven by the angle of attack, it is proposed to add the projected chord length to the "spring" term (cf_{20}) of the second order part. This allows for the desired dependency of stiffness. From Eq. (1) it can be inferred that when projecting the chord perpendicular to the incoming flow this is effectively the same as projecting the Strouhal number. The new equation for cf_{20} will now be:

$$cf_{20} = 10 * projected\_k_s^2 [1 + 3(\Delta c_{l2})^2][1 + 280^2 \tau^2 \dot{\alpha}^2], \tag{18}$$

With:

$$projected_{k_s} = k_s * \sin(\alpha), \tag{19}$$

3.8 Optimization for (Airfoil Specific) Constants

An unconstrained minimization algorithm in MATLAB is used to optimize empirical constants. The algorithm searches for the lowest summation of the absolute errors, from Eq. (13), of all cases considered. The constants selected for this analysis are shown in the initial row of table (2). The constants are chosen as they are in the equations most changed by the improvements. Three optimization analyses have been carried out: a global optimization which covers all cases, an optimization which focussed only on the cases with a mean angle of attack of 14 or 20 degrees, and an optimization has been conducted on the low reduced frequency cases. The initial constants as in table (2) are the start values for the optimization. The results for all individual cases are shown in figure (6). It can be seen that the global optimization is the most optimal. The global optimization gives the most consistently lower error compared to the initial model. In Bladed the Beddoes Leishman dynamic stall model has three sensitive constants which are allowed to be changed by the user. For the Snel model, the optimization shows that two constants are the most sensitive. The optimization output showed significantly different values for these constants for the NACA 4415 and the S809 airfoil. They are shown in the improved row of table (2). These constant will be allowed to be changed by Bladed users. The constants are:

- C1 from table (2). Which will be called the First Order Coefficient
- C2 from table (2). Which will be called the Second Order Forcing Coefficient.

Besides these two the Strouhal number will also be allowed to be changed as different airfoils will have slightly different shedding frequencies.

	Equation	(6)	(16)			(18)	(17)	(17) downstroke
Constant	**Initial**	0.5	0.1	-0.08	1.5	10	280	60	12
	Improved	0.2 ; 0.5 (C1)	0.01	-0.04	1.5 ; 1 (C2)	10	280	60	14

Table 2: Constants used for optimization
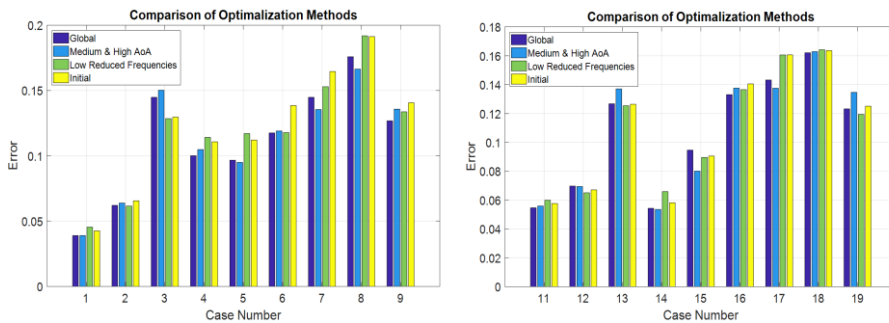
Figure 6: Absolute error analysis of the optimization runs for all cases from table 1.

3.9 Analysis of Shedding Frequency

A first goal of the proposed changes to the Snel model was to capture, predict, and match the vortex shedding and the shedding frequency of airfoils in dynamic stall conditions. In order to check the validity of these changes in a quantitative way a frequency domain analysis has been done. The power spectral density (PSD) estimate is calculated using Welch's method. The Hamming window is set equal to the number of data points and the number of overlapped values to 50% of the window length. The forcing frequency is removed from the plot as the shedding frequencies are higher and the forcing frequency will take up a large proportion of the PSD. The results for both airfoils are shown in figures (7) and (8). From the figures it becomes clear that the Snel model captures, for both airfoils at different mean angles of attack and different reduces frequencies, the self-induced shedding frequencies quite well. All predicted shedding frequencies match frequencies observed in the measurements whereas the intensity isn't always correct. Care must be taken with the higher frequencies as the OSU measurement has a relatively low sampling frequency and might therefore not fully capture some higher frequency dynamics.
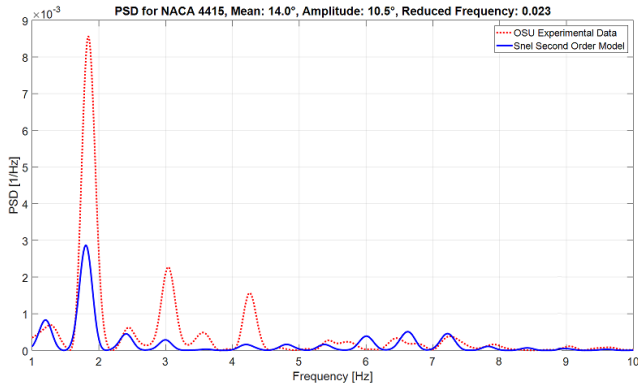
Figure 7: Power spectral density of experimental data and the improved Snel model (NACA 4415 Airfoil at low reduced frequency)
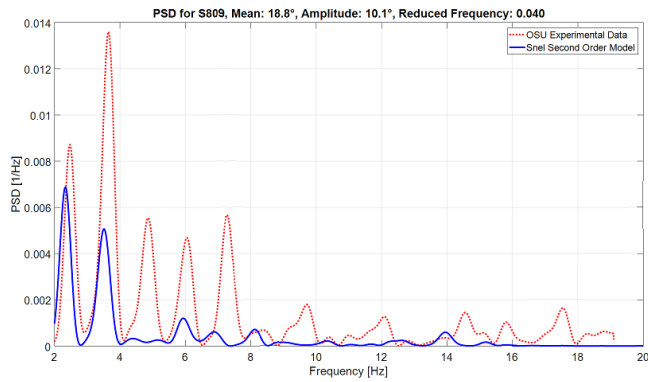
225

Figure 8: Power spectral density of experimental data and the improved Snel model (S809 Airfoil at high reduced frequency)

3.10 Improved Snel Second Order Model

The improved Snel model is quite similar to the original model. The differences lay in the addition of the steady normal force data instead of the steady lift data and the improvements presented in the thesis. The dynamic normal force coefficient is

230 calculated using Eq. (20).

$$c_{n,dyn} = c_{n,steady} + \Delta c_{n1} + \Delta c_{n2}, \tag{20}$$

The modelling of the first order part will follow:

$$\tau \dot{\Delta c}_{n,pot} + cf_{10} \Delta c_{n1} = ft_1, \tag{21}$$

The forcing term ft_1 will be based on the time derivative of the difference between the steady and potential normal force

235 coefficient.

$$ft_1 = \tau \dot{\Delta c}_{n,pot}, \tag{22}$$

$$\Delta c_{n,pot} = c_{n,pot} - c_{n,steady} = c_\alpha \sin(\alpha - \alpha_0) - c_{n,steady}, \tag{23}$$

The potential normal force coefficient slope of Eq. (23), noted as c_α, is calculated similarly as described for the lift coefficient in this paper (see chapter 3.4). The stiffness of the spring coefficient of Eq. (21) is given by Eq. (24). In downwards pitching

240 motion the stiffness is still higher than in upwards pitching motion.

$$cf_{10} = \begin{cases} \frac{1 + C_1 * \Delta c_{n,pot}}{8(1 + 60\tau\dot{\alpha})} & if \ \dot{\alpha} c_{n,pot} \leq 0 \\ \frac{1 + C_1 * \Delta c_{n,pot}}{8(1 + 80\tau\dot{\alpha})} & if \ \dot{\alpha} c_{n,pot} > 0 \end{cases}, \tag{24}$$

The second part of the dynamic lift is again a non-linear mass-damper-spring system following:

$$\tau^2 \Delta \ddot{c}_{n2} + cf_{21} \Delta \dot{c}_{n2} + cf_{20} \Delta c_{n2} = ft_2, \tag{25}$$

The spring and damping coefficients have the same format as the initial model. The empirical constants have been change

245 according to the improvements presented in this thesis. The coefficient are defined as in Eq. (26) and (27) respectively.

$$cf_{20} = 10 * projected\_k_s^2 [1 + 3(\Delta c_{l2})^2][1 + 280^2 \tau^2 \dot{\alpha}^2], \tag{26}$$

$$cf_{21} = \begin{cases} 60\tau k_s [-0.01(\Delta c_{n,pot} - 0.5) + 2(\Delta c_{n2})^2] & if \ \dot{\alpha} > 0 \\ 60\tau k_s [-0.01(\Delta c_{n,pot} - 0.5) + 14(\Delta c_{n2})^2] & if \ \dot{\alpha} \leq 0 \end{cases}, \tag{27}$$

The second order forcing term is defined as:

$$ft_2 = 0.01 k_s \left(-0.04 \Delta c_{n,pot} + C_2 \tau \Delta \dot{c}_{n,pot} \right), \tag{28}$$

250 Where the steady normal force coefficient ($c_{n,steady}$) is the sum of the steady lift and drag coefficient and the angle of attack following Eq. (29) and the steady chordwise coefficient ($c_{c,steady}$) will follow Eq. (30)

$$c_{n,steady} = c_{l,steady} \cos(\alpha) + c_{d,steady} \sin(\alpha), \tag{29}$$

$$c_{c,steady} = -c_{l,steady} \sin(\alpha) + c_{d,steady} \cos(\alpha), \tag{30}$$

When the dynamic normal force coefficient has been obtained an inverse calculation yields the lift and drag coefficients from

255 Eq. (31) and (32).

$$c_{l,dyn} = c_{n,dyn} \cos(\alpha) - C_{c,steady} \sin(\alpha), \tag{31}$$

$$c_{d,dyn} = c_{n,dyn} \sin(\alpha) + C_{c,steady} \cos(\alpha), \tag{32}$$

The First Order Coefficient C_1 will be 0.5 for the NACA 4415 airfoil and 0.2 for the S809. For the Second Order Forcing Coefficient C_2 will be 1 and 1.5 respectively. The results of the improved Snel model are shown in figures (9) and (10). In

260 comparison to figures (2) and (3) it is noted that the shedding prediction at low reduced frequency is improved. For the higher reduced frequency the model also captures the shedding slightly better, even though there is less shedding present. Furthermore, it can be seen that the frequency changes between both cases as desired. It is important to investigate the impact changes on different situations and airfoils. Figure (11) displays the updated model in combination with the S809 airfoil. The improved model still predicts slightly lower values than the experiments but the overall trends are followed nicely and shedding

265 frequency matches the experiment well.
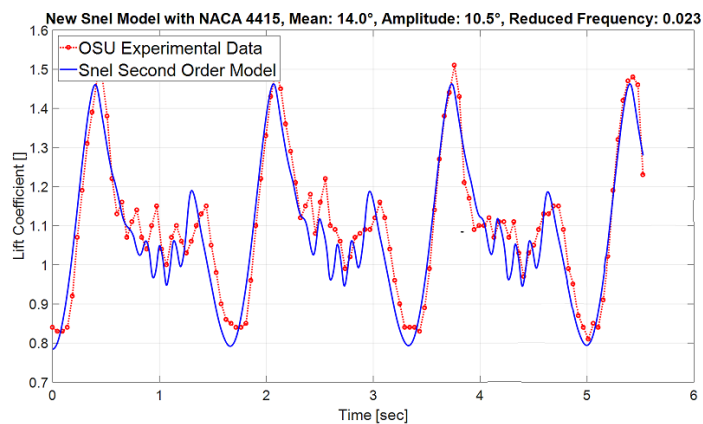
Figure 9: Lift coefficient over time of the improved Snel model (NACA 4415 Airfoil at low reduced frequency)
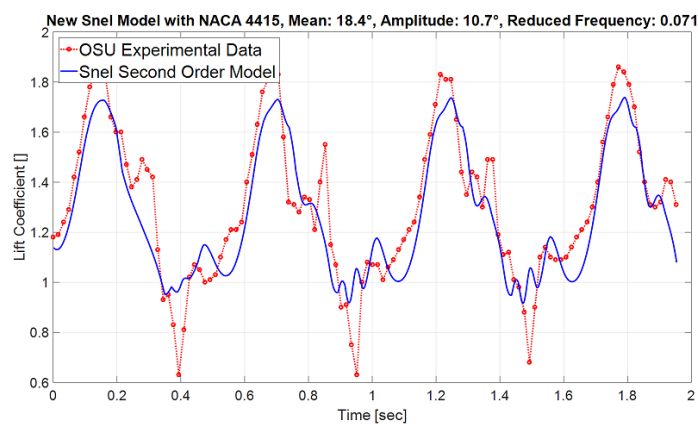
270   **Figure 10: Lift coefficient over time of the improved Snel model (NACA 4415 Airfoil at high reduced frequency)**
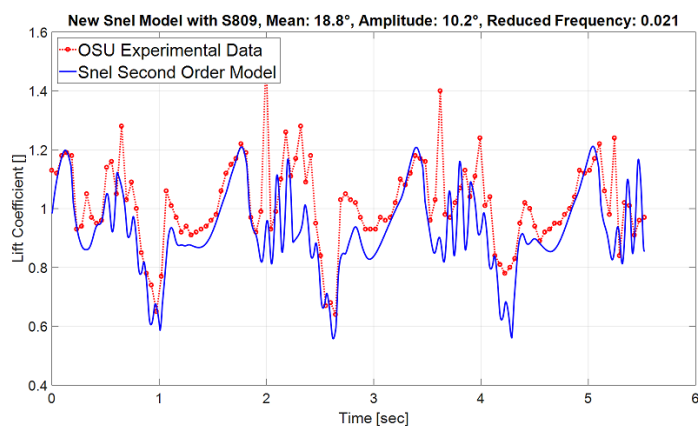
Figure 11: Lift coefficient over time of the improved Snel model (S809 Airfoil at low reduced frequency)

In order to quantify the improvements, the effects of all previous changes on the overall absolute error of the new model are shown in figure (12) together with the overall error of the initial of chapter 3. It is seen that the improved model outperforms
275 the initial on almost every case with a single exception. The initial model already gave very accurate results for that case and the increase in error is very small compared to the reduction achieved in all other cases. It is also noted that the overall prediction of the shedding phenomena has been improved. Hence it can be concluded that the model changes developed and presented in this thesis improve the performance of the Snel second order model.
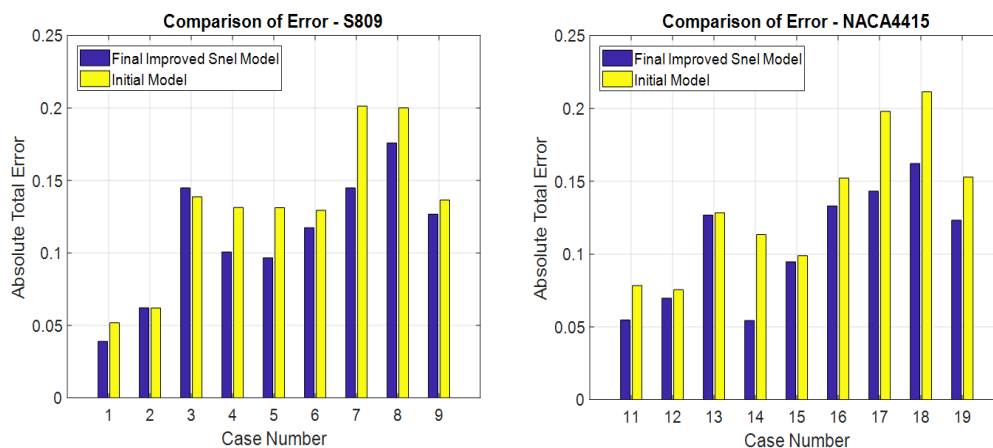
280 **Figure 12: Comparison of the total absolute error of both the initial and improved Snel model**

4. The Snel Model Performance with New MEXICO Data

The Model Rotor Experiments In Controlled Conditions (MEXICO) was a project in which an instrumented, 3 bladed turbine of 4.5m rotor diameter was tested (Schepers and Boorsma et al., 2012). The MEXICO experiments were carried out in the Large Scale Low Speed Facility (LLF) of the German Dutch Wind Tunnels (DNW)(Schepers and Boorsma et al., 2012). The
285 blades were fitted with pressure sensors at 25, 35, 60, 82, and 92% radial positions. Tests were performed with 30m/s wind speed, blades pitched to vane, and yaw inflow angles in the range of -90° to 30° and for three azimuthal positions (0°, 120°, and 240°)**Fout! Verwijzingsbron niet gevonden.**. This data set is particularly valuable for the testing of dynamic stall models as it represents standard load cases set out by the IEC (DNV GL, 2016). For a complete overview of the MEXICO and New MEXICO project reference is made to (Schepers and Boorsma et al., 2012). (Khan, 2018) conducted a similar research with
290 different dynamic stall models and will be used as baseline in this thesis. The improved Snel model from this thesis will be tested against the New MEXICO data sets of table(3) (β = wind direction, θ = pitch angle) to see if the additions and changes to the model have a positive influence on the accuracy. The blade geometry, mass and flexibility distribution are modelled in Bladed according to New Mexico data. The modal damping in the calculations is set to 0.5%. In the runs the rotational augmentation is turned off just like in (Khan, 2018), also the tip and root loss Prandtl corrections are turned off as well as
295 tower shadow effects. 21 blade stations, as in the geometry description of the New Mexico blade, are used. The starting and

ending radius for the dynamic stall model are 25% and 95%. The normal force distribution in axial flow, with pitch -2.3° and thus an angle of attack of 90°, is given in figure (13). The Snel model shows roughly the same size of normal force fluctuations as in the experiment. The improved Snel model predicts shedding at -2.3° pitch with axial flow, due to the addition of the normal force coefficient, while the original model as in (Khan, 2018) does not. The PSD of the time series of both the New

300 Mexico data and the Bladed output are compared. The normal force time series are standardized by subtracting the mean and dividing by the standard deviation. The Hamming window is set to equal the number of data points and the number of overlapped values to 50% of the window length. The results are shown in figure (14) at radial location of 82% of the total span.

Case no.	Case type	Data Point	U [m/s]	β [°]	Θ [°]	Ω [rpm]
1		372	± 30	0	90	0
2		382	± 30	0	75	0
3	Standstill with axial flow	373	± 30	0	45	0
4	(rough)	386	± 30	0	30	0
5		400	± 30	0	12	0
6		375	± 30	0	-2.3	0
7		405, 406, 407	± 30	-90	90	0
8		408, 409, 410	± 30	-60	90	0
9	Standstill with yawed flow	411, 412, 413	± 30	-45	90	0
10	(rough)	414, 415, 416	± 30	-30	90	0
11		420, 421, 422	± 30	15	90	0
12		423, 424, 425	± 30	30	90	0

Table 3: Investigated Cases from the New MEXICO Experiments

305

The updated Snel model shows significantly higher frequency vibrations in the normal force of the New Mexico blade. Figure(15) shows the normal force distribution for the blade at azimuth 120° for the yawed case with 30° wind direction and 90° pitch. Interesting to notice for this case is that the angle of attack will be negative. The Snel model does not show any unsteadiness in the normal force distribution. Further research is needed to explain and improve the Snel model for negative

310 angles of attack.
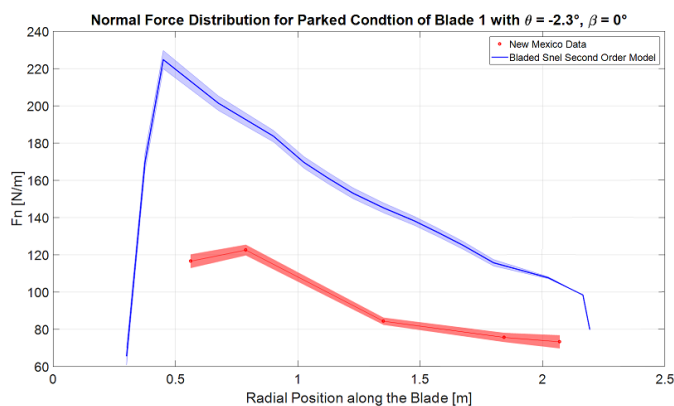
Figure 13: Normal force distribution of the blade at 0° azimuth with -2.3° pitch and 0° wind direction.
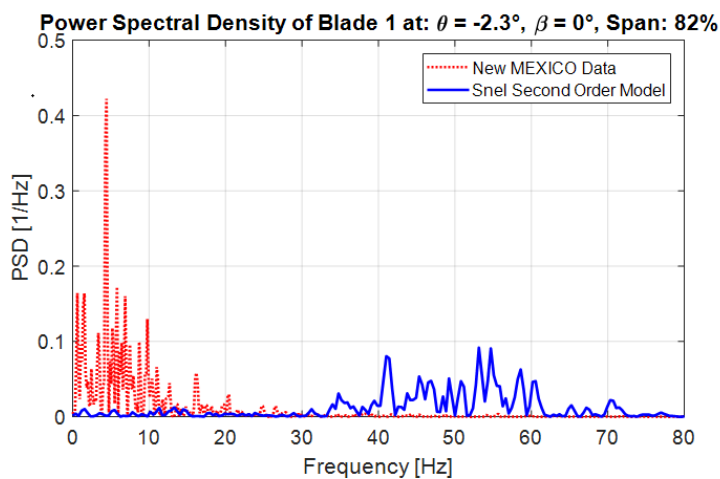
315   **Figure 14:** Power spectral density at 82% span of the blade at 0° azimuth with -2.3° pitch and 0° wind direction.
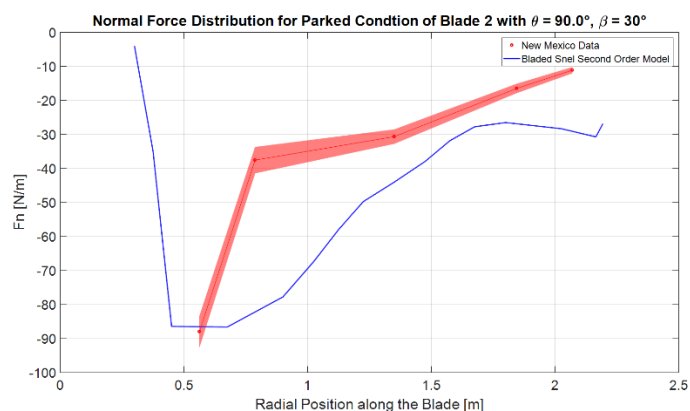
Figure 15: Normal force distribution of the blade at 120° azimuth with 90° pitch and 30° wind direction.

320 A single reason for the higher frequency prediction has not been found. Several possibilities are suggested: First: the modal damping is not specified in the New Mexico turbine data and was therefore assumed as 0.5%. Second: The impact of different airfoils from the New Mexico blade is unknown. The First Order or Second Order Forcing Coefficients might require other values. Furthermore, the Strouhal number for the New Mexico blade is not exactly 0.2 at high angles of attack(Khan 2018). Third: wind tunnel effects are not modelled in Bladed. The wind field in bladed has zero turbulence and wind tunnel effects.

325 More research the Snel model in Bladed with actual turbine data is advised.

5. Conclusion

The Snel model has been validated with OSU experimental data and following this validation propositions for improvements have been made. The improvements to the model have been tested and lead to a reduction in the overall error between the Snel model and the OSU experimental data. Furthermore, an improvement in the prediction of both the amplitude and frequency of

330 vibrations in the measurements has been accomplished. The improved model is implemented in Bladed turbine design software and tested with the New Mexico experimental data. Prediction of normal force distributions along the blade seems to match earlier implementations in other turbine design codes. The Snel model predicts the amplitude of the normal force vibrations well while the predicted frequency is higher than in the experiment. A single reason for this has not been found and therefore further research is advised in to the Snel model. The proposed Snel second order dynamic stall model might become a valuable

335 addition to the modelling of dynamic behaviour in stall conditions. As the conditions tested in this thesis are often design driving, the Snel model looks promising for more accurate prediction of design driving (fatigue) loads and more cost efficient wind turbine designs.

Acknowledgements

The author of this paper would like to express his appreciation to M. Kloosterman and J.G. Schepers for their valuable
340 comments, suggestions and discussions during the research. Without them this thesis would not be possible. The author would also like to thank DNV GL for providing the opportunity to write the thesis within the company. Lastly the association of European Renewable Energy Research Centres, the Hanze University of Applied Sciences, and the National Technical University of Athens are thanked for providing the master's programme.

References

345 Choudry, A. et al.: An insight into the dynamic stall lift characteristics. J. Exp. Thermal and Fluid Science, 58, 188-208, doi:10.1016/j.expthermflusci.2014.07.00, 2014

De Vaal, J.B.: Heuristic modelling of dynamic stall for wind turbines, MSc. Thesis, TU Delft, 2009

DNV GL: Loads and site conditions for wind turbines, Standard DNVGL-ST-0437, 2016

Hoffmann, M.J. et al.: Effects of Grit Roughness and Pitch Oscillations on the NACA 4415 Airfoil, Technical Report
350   NREL/TP-422-7815, https://wind.nrel.gov/airfoils/OSU_data/reports/3x5/n4415.pdf, 1996

Khan, M.A.: Dynamic Stall Modelling for Wind Turbines, MSc. Thesis, TU Delft, uuid:f1ee9368-ca44-47ca-abe2-
b816f64a564f, 2018

Leishman, J.G.: Challenges in modelling the unsteady aerodynamics of wind turbines, J. Wind Energy, 5, 82-132,
doi:10.1002/we.62, 2002

355   McCroskey   W.J.:   The   Phenomenon   of   Dynamic   Stall.:   Technical   Report   NASA-TM-81264,
https://ntrs.nasa.gov/search.jsp?R=19810011501, 1981

Montgomerie, B.: Dynamic Stall Model Called "Simple", Technical Report ECN-C--95-060, 1996.

Pellegrino, A. and Meskell, C.: Vortex shedding from a wind turbine blade at high angles of attack, J. Wind Eng. Ind. Aerodyn.,
121, 131-137, doi:10.1016/j.jweia.2013.08.002, 2013

360   Riziotis, V.A. et al.: Stability analysis of parked wind turbine blades using a vortex model, Conference Science of making
torque from the wind, Heraklion, Greece, 2010.

Schepers J.G. and Snel H.: Model Experiments in controlled conditions, Technical Report ECN-E-07-042, Petten, The
Netherlands, 2007.

Schepers, J.G. and Boorsma, K. et al.: Final report of IEA Task 29, Mexnext (phase 1), Report ECN-E—12-004, 2012

365   Schreck, S. et al.: HAWT Dynamic Stall Response Asymmetries under Yawed Flow Conditions, J. Wind Energy, 3, 215-232,
doi:10.1002/we.40, 2000

Schrek, S.: The NREL Full-Scale Wind Tunnel Experiment, J. Wind Energy, 5, 77-84, doi:10.1002/we.72, 2002.

Snel. H.: Heuristic modelling of dynamic stall characteristics, European Wind Energy Conference, Dublin Castle, Ireland, 429-
433, 1997.

370   Truong, V.K.: A 2-D dynamic stall model based on a HOPF bifuctation, 19th European Rotorcraft Forum Proceedings, C23,
Cernobbio, Italy, 1993.